HHS Public Access

Author manuscript

ACS Nano. Author manuscript; available in PMC 2017 December 30.

Published in final edited form as:

ACS Nano. 2017 September 26; 11(9): 9249–9258. doi:10.1021/acsnano.7b04472.

Dysprosium-Modified Tobacco Mosaic Virus Nanoparticles for Ultra-High-Field Magnetic Resonance and Near-Infrared Fluorescence Imaging of Prostate Cancer

He Hu[†,ID], **Yifan Zhang**[†], **Sourabh Shukla**[†], **Yuning Gu**[†], **Xin Yu**[†], and **Nicole F. Steinmetz**[*,†,‡,§,∥,⊥,ID]

[†]Department of Biomedical Engineering, Case Western Reserve University Schools of Medicine and Engineering, 10900 Euclid Avenue, Cleveland, Ohio 44106, United States

[‡]Department of Radiology, Case Western Reserve University School of Medicine, 10900 Euclid Avenue, Cleveland, Ohio 44106, United States

[§]Department of Materials Science and Engineering, Case Western Reserve University School of Engineering, 10900 Euclid Avenue, Cleveland, Ohio 44106, United States

[∥]Department of Macromolecular Science and Engineering, Case Western Reserve University School of Engineering, 10900 Euclid Avenue, Cleveland, Ohio 44106, United States

[⊥]Division of General Medical Sciences-Oncology, Case Western Reserve University, 10900 Euclid Avenue, Cleveland, Ohio 44106, United States

Abstract

The increasing prevalence of ultra-high-field magnetic resonance imaging (UHFMRI) in biomedical research and clinical settings will improve the resolution and diagnostic accuracy of MRI scans. However, better contrast agents are needed to achieve a satisfactory signal-to-noise ratio. Here, we report the synthesis of a bimodal contrast agent prepared by loading the internal cavity of tobacco mosaic virus (TMV) nanoparticles with a dysprosium (Dy^{3+}) complex and the near-infrared fluorescence (NIRF) dye Cy7.5. The external surface of TMV was conjugated with an Asp-Gly-Glu-Ala (DGEA) peptide *via* a polyethylene glycol linker to target integrin $\alpha_2\beta_1$. The resulting nanoparticle (Dy-Cy7.5-TMV-DGEA) was stable and achieved a high transverse relaxivity in ultra-high-strength magnetic fields (326 and 399 mM^{-1} s^{-1} at 7 and 9.4 T, respectively). The contrast agent was also biocompatible (low cytotoxicity) and targeted PC-3 prostate cancer cells and tumors *in vitro* and *in vivo* as confirmed by bimodal NIRF imaging and

[*]**Corresponding Author**: nicole.steinmetz@case.edu.

[ID]**ORCID**

He Hu: 0000-0002-5976-5273

Nicole F. Steinmetz: 0000-0002-0130-0481

Supporting Information

The Supporting Information is available free of charge on the ACS Publications website at DOI: 10.1021/acsnano.7b04472. Mass spectrometry, absorption and NIRF emission spectrum, Job curve of the fluorescence intensity of Cy7.5 *vs* concentration, binding affinity (K_d), comparison of $r_{1,2}$ relaxivity of Dy^{3+}-based nanoparticles, relationship of r_2 as a function of the square of magnetic field (B^2) (PDF)

Notes

The authors declare no competing financial interest.

T_2-mapping UHFMRI. Our results show that Dy-Cy7.5-TMV-DGEA is suitable for multiscale MRI scanning from the cellular level to the whole body, particularly in the context of UHFMRI applications.

Graphical Abstract

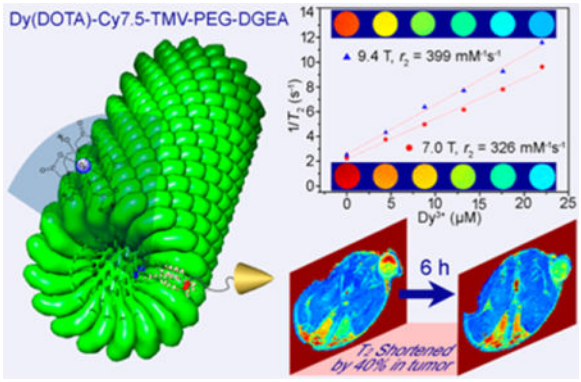

Keywords

dysprosium; tobacco mosaic virus; ultrahigh-field magnetic resonance imaging; near-infrared fluorescence imaging; prostate cancer

Magnetic resonance imaging (MRI) is one of the most powerful and versatile noninvasive imaging techniques and is widely used for biomedical research and clinical diagnosis. The spatial and temporal resolution of MRI increases in stronger magnetic fields (≥3.0 T) resulting in higher signal-to-noise ratios.[1–3] Preclinical MRI studies in small animal models often utilize ultrahigh field strengths (≥7.0 T).[2,3] The relatively low signal-to-noise ratio of normal tissues is improved using contrast agents, which selectively reduce the T_1 or T_2 relaxation times in the region of interest to enhance the signal.[3] Contrast agents are currently used in ~35% of clinical MRI scans, but this is expected to increase as the next generation of multifunctional MRI contrast agents become more widely available.[4] The efficiency of a contrast agent is determined by its r_1 ($1/T_1$) or r_2 ($1/T_2$) relaxivity (the relaxation enhancement of solvent water protons caused by the presence of the relaxation enhancer at a concentration of 1 mM) as well as the r_2/r_1 ratio. As the r_2/r_1 ratio increases, the substance becomes a more efficient T_2 contrast agent and a less efficient T_1 contrast agent, and *vice versa*.[3] Whereas gadolinium-(III) ion (Gd^{3+})-based T_1 contrast agents are efficient in low-strength magnetic fields, the longitudinal relaxivity is rapidly lost at higher field strength,[5,6] declining by as much as 30%.[3,5,7] T_2 contrast agents such as superparamagnetic iron oxide nanoparticles (SIONPs) have many advantages in both biomedical research and preclinical applications,[8] but ultrahigh magnetic fields result in aggregation, movement, and saturated magnetization obstacles that limit the ability to distinguish genuine signals from background.[3,9] As ultrahigh-field scanners become more widely available, new contrast agents are required to ensure a high signal-to-noise ratio can be achieved without the limitations described above.

Unlike classic Gd^{3+} contrast agents, the paramagnetic dysprosium(III) ion (Dy^{3+}) has the shortest electronic relaxation time (τ_e = 0.5 ps) and highest effective magnetic moment (μ_{eff} = 10.6 μB) among the lanthanide ions, affecting proton relaxivity *via* a Curie mechanism that primarily influences T_2.[10,11] The contribution of Curie relaxation increases substantially with the external magnetic field and is proportional to the square of the magnetic moment of the lanthanide ion, which results in highly efficient r_2 relaxation in ultrahigh-field MRI (UHFMRI) applications. Although a small number of Dy^{3+} chelates (e.g., Dy^{3+}-DTPA)[12–14] and inorganic nanoparticles (*e.g.*, Dy_2O_3 and $NaDyF_4$)[3,15,16] have been studied as potential T_2 contrast agents, no further biological applications have been reported. Generally, nanoparticle contrast agents offer more advantages than small molecular chelates. Nanoparticles have uniform shapes and sizes and surfaces that can be functionalized to prolong circulation, target particular cells, and carry drugs or imaging agents.[11] The advantages of both metal complexes and nanoparticles can be combined by optimizing the relaxivity of metal complexes confined within nanoparticles,[9,10,17] such as dendrimers,[18] polymers,[19,20] silica,[6,21] protein cages, viral nanoparticles (VNPs), or virus-like particles (VLPs).[22,23]

VNPs and VLPs, especially those based on plant viruses and bacteriophages, are remarkably versatile due to their high degree of symmetry, polyvalency, monodispersity, and genetic or chemical programmability.[24] Using chemoselective bio-conjugation, VNPs and VLPs can be functionalized with imaging contrast agents, drugs, and/or targeting ligands such as peptides or antibodies.[24] Rodlike plant viruses such as the virions of tobacco mosaic virus (TMV) are particularly versatile because the high aspect ratio shape confers superior properties. The TMV nanoparticles' capsid comprises 2130 identical coat proteins that self-assemble into a 300 × 18 nm hollow tube with a solvent-accessible 4 nm interior channel with the viral ssRNA.[25] The benefits of such rodlike particles include more effective evasion of the immune system, particularly the mononuclear phagocyte system, and more efficient margination toward the blood vessel wall to improve extravasation.[26,27] TMV is biocompatible and biodegradable and does not cause infections in humans, allowing multiple nanomedical applications: for example, we have recently developed Gd(DOTA)-conjugated TMV nanoparticles for the imaging of atherosclerotic plaques[22,23] and TMV carriers for the delivery of phenanthriplatin to cancer cells.[28]

Here, we aimed to determine whether the immobilization of Dy^{3+}(DOTA) on the internal surface of the TMV nanotube offers an alternative strategy for the development of contrast agents with high transverse relaxivity for UHFMRI, using prostate cancer imaging as a case study. Prostate cancer is the sixth most common cancer in the world and the third most common in men, especially in Europe and North America.[29–31] Among human prostate cancer cell lines, PC-3 is more aggressive and expresses higher levels of integrin $\alpha_2\beta_1$ on the surface than cell lines CWR-22 and LnCap. The $\alpha_2\beta_1$ integrin is a receptor for type I collagens, laminins, E-cadherin, matrix metalloproteinase 1, and several viruses,[32] and its signaling activity is modulated during the initiation and progression of prostate cancer, making it an important diagnostic marker and therapeutic target. We have previously demonstrated that the peptide Asp-Gly-Glu-Ala (DGEA) can be used as a targeting ligand to visualize integrin $\alpha_2\beta_1$ expression *in vivo*.[33] Fluoromagnetic nanomaterials with multifunctional properties have recently attracted attention due to their special coupled

behaviors.[33] A single nanoparticle combining the high sensitivity of fluorescence and UHFMRI imaging would be suitable for multiscale scanning, from the cellular level to the whole body. Our bimodal design combines a near-infrared fluorescence (NIRF) dye and Dy^{3+}(DOTA) loaded into the internal channel of TMV nanoparticles displaying external DGEA peptides for the targeting of prostate cancer cells. We tested the feasibility of this contrast agent for the imaging of prostate cancer cells *in vitro* and *in vivo*.

RESULTS AND DISCUSSION

Synthesis and Characterization of Dy-Cy7.5-TMV-DGEA

As shown in Scheme 1A, the TMV nanoparticle comprises 2130 identical coat protein subunits which self-assemble into an elongated nanotube (300 × 18 nm) with a 4 nm internal channel with the viral ssRNA. The high-resolution crystal structure of TMV highlights an internal glutamic acid residue (GLU97/106, blue) and an external tyrosine residue (TYR139, red) that can be functionalized using the well-established copper-catalyzed azide–alkyne cycloaddition (CuAAC) strategy, also known as click chemistry.[23,34] The TMV nanoparticle is propagated in and isolated from *Nicotiana benthamiana* plants, which are inexpensive to grow and highly scalable. The internal surface is modified with alkyne handles then conjugated with the macrocyclic MRI contrast agent Dy-DOTA-azide (azido-monoamide-1,4,7,10-tetraazacyclododecane-*N*,*N*′,*N*″,*N*‴-tetraacetic acid, Figure S1) and the NIRF dye Cy7.5-azide (Scheme 1B). The external surface is modified with alkyne handles then conjugated with mPEG-azide to generate untargeted control particles (Dy-Cy7.5-TMV-mPEG) or the DGEA peptide (*via* a heterofunctional azide-PEG-maleimide linker) to generate targeted particles (Dy-Cy7.5-TMV-DGEA) that bind to integrin $\alpha_2\beta_1$ on the surface of PC-3 prostate cancer cells (Scheme 1C).

The morphology of the particles after each modification step was observed by transmission electron microscopy (TEM) as shown in Figure 1A–C. The native TMV nanoparticles show the typical elongated nanostructures (Figure 1A). After internal and external modification, the Dy-Cy7.5-TMV-mPEG (Figure 1B) and Dy-Cy7.5-TMV-DGEA (Figure 1C) particles remained structurally sound, showing the elongated nanotube shape. The order of chemical reactions was important to ensure particle integrity and stability. Specifically, we modified the interior first and then the exterior to ensure that all contrast agents were sequestered inside the particle and to avoid particle aggregation. Size-exclusion chromatography (SEC) showed that all particles eluted at ~7.4 mL, confirming that the modification did not cause particle degradation or aggregation (Figure 1D). Successful surface modification was confirmed by denaturing sodium dodecyl sulfate polyacrylamide gel electrophoresis (SDS-PAGE) and Western blotting, using antibodies against polyethylene glycol (PEG) (Figure 1E,F). The TMV coat protein (M_r = ~17 kDa) was present in all samples. After conjugation with Cy7.5 (M_r = 767.44 Da), Dy(DOTA) (M_r = 646.16 Da), and PEG (M_r = ~2000 Da), the Dy-Cy7.5-TMV-mPEG and Dy-Cy7.5-TMV-PEG-Mal particles were represented by an additional band of ~20 kDa corresponding to the anticipated increase in mass of the coat protein monomer. Following the further conjugation of Dy-Cy7.5-TMV-PEG-Mal with the DGEA peptide (M_r = 493.4 Da), the ~20 kDa band disappeared and was replaced with a ~38 kDa band, suggesting that the preferred conformation was a dimer, perhaps reflecting the

intertwining of the PEG chains.[35] Western blotting confirmed that PEG was present in both the ~20 and ~39 kDa bands. Further densitometric analysis of the particles indicated ~65% coverage with mPEG, ~50% coverage with the PEG-Mal linker, and ~20% coverage with the DGEA peptide.

The density of TMV coat protein labeling with Cy7.5 and Dy(DOTA) was quantified by UV/vis spectrophotometry (Figure S2) and inductively coupled plasma optical emission spectroscopy (ICP-OES), respectively. The loading efficiency depends on the carbodiimide coupling reaction, so we loaded a smaller quantity of dye than the fluorescence quench concentration (Figure S3) combined with maximum Dy-(DOTA) loading to achieve the strongest MRI signal. We found that TMV loaded with ~380 Cy7.5 molecules and ~980 chelated Dy^{3+} ions, covering ~18% and ~46% of the available internal surface, respectively, satisfied our requirements.

Relaxivity of Dy-Cy7.5-TMV-mPEG at 7 and 9.4 T

The transverse relaxivity (r_2), longitudinal relaxivity (r_1), and r_2/r_1 ratio of the Dy-Cy7.5-TMV-mPEG nanoparticles in different magnetic fields (1.5, 7, and 9.4 T) were measured as shown in Figure 2A–C. The r_2 values of the nanoparticles were 62, 326, and 399 mM^{-1} s^{-1} at 1.5, 7, and 9.4 T, respectively, which is significantly higher than alternatives such as Dy_2O_3 nano-particles (190 mM^{-1} s^{-1} at 7.0 T) and $NaDyF_4$ nanoparticles (101 mM^{-1} s^{-1} at 9.4 T).[3,16] The r_2 relaxivity of our nanoparticles was also much higher than that of Dy^{3+} chelates, *e.g.*, ~33 times higher than complexes such as Dy^{3+}-DOTA-$(Gly)_3$ (~12 mM^{-1} s^{-1} at 9.4 T).[36] The contrast in T_2-weighted MRI depends on the r_2 value, and the higher the r_2/r_1 ratio, the more efficient the T_2 contrast agent. The r_2/r_1 ratios of our nanoparticles were 6.7, 155, and 160 at 1.5, 7, and 9.4 T, respectively, which is much higher than commercial Feridex (r_2/r_1 = 22 at 3 T),[37] indicating that our nanoparticles are excellent candidate T_2 contrast agents for UHFMRI applications.

The diamagnetic contribution to the relaxivity is negligible for water protons, and the contact effect is transmitted through chemical bonds by scalar coupling between the unpaired electrons and the nuclear spins, which is much smaller than the dipolar and Curie contributions for the lanthanides (except Gd^{3+}) and is thus negligible.[3,10] The dipolar component is a spatial effect resulting from dipolar coupling between the spin of unpaired electrons of the lanthanide ion and nuclear spins, and is described by the Solomon–Bloembergen–Morgan (SBM) equations.[38,39] The Curie component, or Curie spin relaxation, arises from the dipolar interaction of the nuclei with the thermal average of electron-spin polarization.[40,41] Curie spin relaxation becomes an important contributor to water proton relaxivity when the electronic relaxation time (τ_{1e}) of the paramagnetic ion is short enough to allow for spins to return to their thermal equilibrium before the molecule changes position, which is described as the rotational correlation time (τ_R). In the case of Dy^{3+}, τ_{1e} = ~ 0.5 ps. In other words, the lanthanide complex must be almost immobile during the interval τ_{1e}, which can be achieved by conjugating the complex to nanoparticles.[10] For example, τ_R = ~10^{-10} s in small lanthanide complexes such as Ln-DTPA, but this increases dramatically on the nanosecond scale following conjugation to nanoparticles.[6] The dipolar and Curie components are therefore major contributors to the

relaxivity enhancement achieved by Dy(DOTA)-modified TMV nano-particles. According to the well-established relaxivity theory, the transverse relaxivity of UHFMRI contrast agents should increase linearly with the square of the external magnetic field strength B and the static correlation time $1/\Delta\omega$, where $\Delta\omega$ is the difference between the Larmor frequency at the particle surface and at infinity.[42] The transverse relaxivity is shown as a function of B^2 and $\Delta\omega$ is shown as a function of B in Figure S4A,B. The corresponding power functional relationship shows a sharp jump from intermediate (1.5 T) to ultrahigh (7 and 9.4 T) field strengths. These results confirm that the SBM effect contributes to the relaxivity of our nanoparticles in an intermediate-strength field, but the Curie component dominates the relaxivity in an ultrahigh-strength field, suggesting our nanoparticles would be ideal as UHFMRI contrast agents.

Finally, to demonstrate the feasibility of our nanoparticles for UHFMR imaging, concentration-dependent T_2-mapping phantom images of the Dy-Cy7.5-TMV-mPEG water solutions were obtained at 7 and 9.4 T (Figure 2D,E). Both series of images show a clear concentration-dependent negative contrast gradient produced by the nanoparticles, confirming their suitability for UHFMRI applications.

Targeted *in Vitro* Bimodal Imaging Using TMV-Based Contrast Agents

The *in vitro* biocompatibility of the targeted particles (Dy-Cy7.5-TMV-DGEA) and untargeted control particles (Dy-Cy7.5-TMV-mPEG) was assessed using the methylthiazolyltetrazolium (MTT) assay in human prostate cancer cell line PC-3 (Figure 3). The viability of untreated cells was used as the blank. No significant reduction in cell viability (>95%) was observed when PC-3 cells were incubated at 37 °C with either of the nanoparticle preparations at concentrations of 0.1–0.4 mg/mL for 12 or 24 h. Notably, cell viability remained >92% even after 24 h incubation with 0.4 mg/mL of the nanoparticles, the highest concentration we tested. The low *in vitro* cytotoxicity of these nanoparticles suggests they are likely to be suitable for *in vivo* imaging.

To evaluate the feasibility of the particles for cancer cell detection by NIRF and MRI, PC-3 cells were incubated for 3 h at 37 °C with different concentrations of Dy-Cy7.5-TMV-mPEG or Dy-Cy7.5-TMV-DGEA (0.1, 0.2, 0.3, and 0.4 mg/mL) and then immobilized in agarose. A concentration-dependent NIRF signal was observed in cells treated with either the control or the targeted nanoparticles, but the signal generated by the targeted particles was higher at all concentrations, and as much as 1.5-fold higher at the maximum concentration of 0.4 mg/mL (Figure 4A,B). Similarly, a T_2-mapping MRI scan revealed that the nanoparticles reduced the normalized T_2 value in a concentration-dependent manner, with the targeted nanoparticles achieving a 7-fold greater effect at a concentration of 0.1 mg/mL (~20% *vs* ~3% reduction) and a 2-fold greater effect at a concentration of 0.4 mg/mL (~27% *vs* ~11% reduction) (Figure 4C,D). The amount of Dy^{3+} taken up by PC-3 cells per milligram of protein was quantified by ICP-OES and the Bradford protein assay, revealing a concentration-dependent range of 120–230 pmol Dy^{3+}/mg protein for the targeted nanoparticles compared to 44–100 pmol Dy^{3+}/mg protein for the control nanoparticles (Figure 4E). Based on the Dy^{3+} loading ratio of 46%, the efficiency of particle uptake was 32–57% for the targeted particles and 11–25% for the control particles. The observed 2–3-

fold difference in uptake efficiency matched well with the faster T_2 relaxivity, and the greater difference at lower particle concentrations emphasized the advantage of targeting ligands. Even so, the control particles still achieved relatively efficient passive uptake into cancer cells, consistent with earlier reports that elongated nanoparticles pass through cell membranes more effectively than spherical nanoparticles due to their high degree of curvature.[23,26,27]

We determined the binding affinity of the Dy-Cy7.5-TMV-DGEA to PC-3 cells and found that the specific binding affinity constant (K_d) of Dy-Cy7.5-TMV-DGEA to PC-3 cells lies at 71.5 nM, which is at the same rank order of that of antiprostate specific membrane antigen (PSMA) monoclonal antibody (35.6–46.5 nM) (Figure S5).[43] Therefore, our Dy-Cy7.5-TMV-DGEA nanoparticles appear to bind $\alpha_2\beta_1$ integrin efficiently *in vitro*.

Targeted *in Vivo* Bimodal Imaging and ex Vivo Biodistribution Studies

Having confirmed the ability of Dy-Cy7.5-TMV-DGEA nanoparticles to target $\alpha_2\beta_1$ integrin on the surface of human PC-3 prostate cancer cells *in vitro*, we proceeded to test their ability to target PC-3 tumors *in vivo* in mouse models by bimodal NIRF imaging and T_2-mapping MRI. Accordingly, athymic nude mice ($n = 3$) with xenografted human prostate tumors were scanned before particles injection and at 1, 6, and 24 h after injection.

Quantitative NIRF imaging was carried out by measuring fluorescence intensities, defined as photons per second per centimeter squared per steradian (p/s/cm^2/sr), and normalizing them to the same scale bar in the whole-body image as a function of time (Figure 5A). Maximum uptake into tumor tissue was observed 6 h postinjection, followed by gradual washing out. In contrast, rapid uptake into other tissues (such as liver and spleen) was observed after 1 h postinjection. We also detected a signal in the lymph nodes 6 h postinjection which had declined slightly by 24 h postinjection, indicating that the nanoparticles remained in circulation for a significant length of time. The enhancement of the signal in the tumor was quantified in complete tumor cross sections, using preinjection mice as background controls normalized to 100%. The signal intensity in the PC-3 tumor region had increased by ~2.5-fold ($p < 0.05$) 6 h postinjection (Figure 5B) and declined slightly thereafter, but remained ~2-fold ($p < 0.05$) higher than the control 24 h postinjection (Figure 5B). The *ex vivo* NIRF images (Figure 5C) clearly show the changes in fluorescence intensity between the dissected tumor and other tissues. Compared to the blank control and nontargeted nanoparticles, the targeted nanoparticles achieved a significant increase in fluorescence. The semiquantitative biodistribution data agreed with the *ex vivo* and *in vivo* NIRF images (Figure 5D).

MRI imaging was performed to determine the impact of the targeted and untargeted nanoparticles on the T_2 relaxation times of local tissues. As the T_2 relaxation time declines, the color of the T_2 MR images changes from red to blue, as shown in the scale bar (Figure 6A), reflecting the accumulation of contrast agents. The quantitative analysis of T_2 relaxation times (Figure 6B) revealed only a slight signal enhancement 1 h postinjection compared with the preinjection background, probably because only a limited number of Dy^{3+}(DOTA)-conjugated TMV nanoparticles enter the tumor site within this short time while most remain in circulation, unlike small molecular contrast agents which usually achieve maximum signal enhancement within 1 h.[9,11] Accordingly, much stronger signal

enhancement was achieved by the targeted particles 6 h postinjection (~40%) compared with the control particles (~14%) and both treatment groups showed a recovery of T_2 relaxation times 24 h postinjection, reflecting the biodegradation and clearance of nanoparticles from the mice. The rapid clearance of contrast agents after MRI is a desirable property, and the biodegradable, proteinaceous TMV-based particles may be advantageous in this context over synthetic and metallic contrast agents, which can persist in the body for long periods of time.[44,45]

Prostate cancer is typically seen as an island of low signal intensity (indicative of a shorter T_2 relaxation time constant for tumor) enclosed by high signal intensity (longer T_2) from surrounding benign peripheral tissue.[46] However, MRI typically requires a long spin-echo time (TE) to obtain sufficient tumor-to-normal prostate contrast because of a limited relaxation time constant differential between benign and neoplastic tissue. To date, there is only a limited number of reports on quantitative MRI *in vivo*. In one example, the prostate-specific membrane antigen (PSMA) peptides conjugated Gd-DOTA complex was used for targeting MR imaging of prostate cancer with PC-3 tumor model.[47] The results showed average 36% enhancement in R_1 values in the first 40 to 60 min postinjection using targeted formulations. However, the highest contrast enhancement in the control group was approximately 24% at 20 min post injection, followed by a rapid decay in contrast enhancement. In the case of iron oxide based T_2 MRI contrast agents, here using Gd-DTPA modified ultrasmall magnetic iron oxide nanoparticles for liver imaging, the results demonstrated that the signal from T_1-weighted MRI was positively enhanced by 26% based on the Gd-DTPA moiety, and negatively decreased by 20% from the iron oxide nanoparticles, respectively.[48] In a different study, folate-targeted super-paramagnetic iron oxide nanoparticles enabled cervical tumor imaging in a mouse model with T_2-weighted MR signals decreased by 20–25%.[49] In comparison, in this work, we showed that 6 h post administration of the TMV-based contrast agent, the tumor T_2 value dropped by 40% using the DGEA-targeted particles, compared with only 14% decrease in the nontargeted control group. Therefore, compared to previous literature examples, our results stand out and highlight the potential of TMV as a contrast agent for UHFMRI.

The dose of our contrast agent in terms of Dy^{3+} ions was 5 μmol/kg, which is 200 times lower than typical T_1 contrast agents (0.1 mmol/kg for Prohance, which is the most similar formulation), and 20 times lower than commercial T_2 contrast agents (0.01 mmol/kg for Feridex, which is based on Fe^{3+} ions).[50] Even so, we achieved significant contrast enhancement at these low doses, reflecting two key properties of our nanoparticles: the high r_2 relaxivity (326.0 mM^{-1} s^{-1}) and r_2/r_1 ratio (155) in ultrahigh-strength magnetic fields (7 T), and the ability of the DGEA peptide ligands to target specific cells.

To confirm the biodistribution of our nanoparticles in normal organs and tumors, the Dy^{3+} content was determined by ICP-OES (Figure 6C). In agreement with the *in vivo* MRI data, more Dy^{3+} accumulated in the tumors of mice treated with the targeted nanoparticles (86 ng) than those treated with the control particles (49 ng). Relatively large numbers of particles also accumulated in the liver in both treatment groups, which is expected given that nanoparticles are taken up from the circulation by the mononuclear phagocytic system. Some particles also accumulated in the lung, perhaps due to particle agglomeration caused

by the adsorption of plasma proteins,[21,51] but also probably due to the targeting of $\alpha_2\beta_1$ integrin which is expressed in healthy lung tissue.[52–54] The kidneys accumulated similar levels of Dy^{3+} to the tumor tissue, consistent with their role as an excretory pathway for nanoparticles. Collectively, our *in vivo* results confirmed that Dy-Cy7.5-TMV-DGEA particles can be used as efficient NIRF/T_2-UHFMRI bimodal contrast agents for *in vivo* applications.

CONCLUSIONS

We investigated the properties of Dy^{3+}(DOTA)/Cy7.5-conjugated TMV bimodal contrast agents and confirmed their high transverse relaxivity in ultrahigh-strength magnetic fields, which is mainly dependent on the Curie mechanism. Our systematic *in vitro* and *in vivo* studies demonstrated that the targeted Dy-Cy7.5-TMV-DGEA nanoparticles are suitable for both NIRF imaging and T_2-mapping MRI in the context of prostate cancer cells, and could therefore serve as a bimodal contrast agent for both fluorescence imaging and UHFMRI. Importantly, our proof-of-principle approach confirmed that the robust molecular structure of TMV offers a versatile platform for future theranostic applications.

EXPERIMENTAL SECTION

TMV Bioconjugation

Wild-type TMV nanoparticles were propagated in *N. benthamiana* plants and isolated from plant extracts by chloroform: butanol extraction and ultracentrifugation as previously described.[24] The virus concentration in plant extracts was determined by UV/vis spectrophotometry ($\varepsilon_{260\ nm}$ = ~3.0 $mLmg^{-1}cm^{-1}$). The Dy-Cy7.5-TMV-mPEG and Dy-Cy7.5-TMV-DGEA nanoparticles were synthesized using a combination of carbodiimide coupling (targeting internal glutamic acid residues) and diazonium coupling (targeting external tyrosine side chains) to introduce alkyne ligation handles, followed by the introduction of Cy7.5 and Dy-DOTA as contrast agents and the Asp-Gly-Glu-Ala (DGEA) peptide using copper-catalyzed azide–alkyne cycloaddition (CuAAC) and thiol–maleimide Michael addition reaction chemistry (see the Supporting Information).

Particle Characterization

Particle integrity was confirmed by TEM and SEC. Bioconjugation was confirmed by SDS-PAGE and Western blotting (see the Supporting Information). The concentration of nanoparticles was determined using a standard Bradford assay followed by measuring the absorbance on a NanoDrop 2000 spectrophotometer (Thermo Fisher Scientific, Waltham, MA). The ionic relaxivity of the particles was tested at 37 °C using a Brukman Minispec mq60 relaxometer (60 MHz) and a BioSpec 70/30USR preclinical 7.0 T (300 MHz) and 9.4 T (400 MHz) MRI (Bruker Inc., Billerica, MA). The concentration of Dy^{3+} ions was determined by 730-ES ICP-OES (Agilent Technologies, Santa Clara, CA).

Cell Culture and Cytotoxicity

The human prostate cancer cell line PC-3 was maintained at 37 °C in a humidified 5% CO_2 atmosphere. The cells were grown in RPMI-1640 medium (Corning Life Sciences, New

York, NY) with 10% fetal bovine serum (Atlanta Biologicals, Flowery Branch, GA) and 1% penicillin–streptomycin (Thermo Fisher Scientific). The *in vitro* cytotoxicity of the nanoparticles was evaluated using the MTT cell proliferation assay (ATCC 30-1010K). We seeded 5×10^4 cells/well into a 96-well cell culture plate and incubated it as described above for 24 h. We then added different concentrations of the nanoparticles (0, 0.1, 0.2, 0.3, and 0.4 mg/mL) and incubated it for a further 12 or 24 h as above. We then added 10 μL of MTT to each well, and the plate was incubated for an additional 2–4 h until a purple precipitate became visible. We then added 100 μL/well of Detergent Reagent and incubated the contents at room temperature in the dark for 2 h before reading the OD_{570} absorbance on a Infinite 200 microplate reader (Tecan, Männedorf, Switzerland). The following formula was used to calculate the inhibition of cell growth:

$$\text{cell viability } (\%) = \left(\frac{\text{mean absorbance value of treatment group}}{\text{mean absorbance value of control}} \right) \times 100$$

In Vitro NIRF Imaging and MRI of PC-3 Cells

Approximately 2×10^5 PC-3 cells were seeded per well into 24-well plates and incubated as above overnight. We then added different concentrations of the nanoparticles (0, 0.1, 0.2, 0.3, and 0.4 mg/mL, equivalent to 0, 1×10^6, 2×10^6, 3×10^6, and 4×10^6 particles/cell, diluted in PBS) and incubated for 3 h as above. The cells were then washed three times with PBS, detached with trypsin/EDTA, transferred to Falcon tubes and fixed with 25% agarose. *In vivo* NIRF imaging was carried out using an IVIS 200 small-animal imaging system (Xenogen, Alameda, CA). A Cy7.5 filter set was used to acquire the Cy7.5 signal. Identical illumination settings (lamp voltage, filters, f/stop, field of views, binning) were used to acquire all images, and fluorescence emission was normalized to photons per second per centimeter squared per steradian (p/s/cm^2/sr). Images were acquired and analyzed using Living Image v2.5 software (Xenogen).

The *in vitro* MRI studies were carried out using a horizontal Biospec 7 and 9.4 T scanners equipped with a 3 cm birdcage ^{1}H coil (Bruker, Erlangen, Germany). First, a multislice, T_2 weighted imaging sequence (RARE) was used to provide location information on the cells or tumor with the following parameters:[55] TE/TR = 24/3000 ms, RARE factor = 8, NAV = 1, 15 axial slices with 1.5 mm thickness, matrix size = 128 × 128, 30 × 30 mm field of view (FOV). Total acquisition time was 48 s. Next, a single slice, T_2-mapping Carr–Purcell–Meiboom–Gill sequence was optimized to detect the boundary of the lesions at the xenograft site with the following parameters:[56] TE = 8, 16, 24...512 ms (64 echoes), TR = 1000 ms, NAV = 2, 1.5 mm thickness, matrix size = 128 × 128, 30 × 30 mm FOV. Total acquisition time was 4 min 16 s. After imaging, the cell samples were collected and sonicated at 30% power for 30 s in ice, and the total protein content was measured using the Quick Start Bradford Protein Assay with bovine serum albumin as standard (Biorad, Hercules, CA). Next, the reset cell samples were digested with concentrated hot HNO_3 and the Dy content was determined by ICP-OES as described above.

Tumor Xenografts

Animal experiments were performed according to IACUC-approved procedures at Case Western Reserve University. Male athymic nude mice (NCR *nu/nu*), obtained from Case Western Reserve University Athymic Core at 4–6 weeks of age (25–30 g), were injected subcutaneously in the right shoulder with 1×10^6 PC-3 human prostate cancer cells suspended in 100 μL RPMI medium and Matrigel (Corning Life Sciences) at a 1:1 ratio. Once established, tumors were monitored daily. The mice were analyzed when the tumors reached 80–100 mm^3 (14–21 days postinjection).

In Vivo NIRF Imaging and MRI

Mice were anesthetized for all procedures (isoflurane 2.5%; O_2 2.0 L/min), and their respiration, body temperature, and heart rate were monitored in real time. They were scanned before and 1, 6, and 24 h after the injection of 200 μL of nanoparticles in PBS through the tail vein (n = 3 for each time point, dose = 20 mg/kg).

At each time point, mice were first visualized by *in vivo* NIRF imaging (as described above for the *in vitro* experiments) and then by *in vivo* MRI using a 7 T system for T_2-mapping studies. The parameters used for *in vivo* MRI are as the same as the *in vitro* scan. During MR imaging, mice were anesthetized by isoflurane, and their respiration rate was maintained at 70–80/min. Images were acquired before and after injection. T_2 maps were statistically analyzed using in-house developed Matlab software (Natick, MA).

The tumor and major organs (brain, lung, heart, liver, spleen, and kidneys) were removed, and *ex vivo* fluorescence images were obtained as above. The tissues were weighed and digested in concentrated nitric acid overnight and heated to 90 °C for a further 6 h before the Dy content was determined by ICP-OES. Values are presented as means plus standard deviations for $n = 3$ mice per group.

Supplementary Material

Refer to Web version on PubMed Central for supplementary material.

Acknowledgments

This work was funded by a grant from the National Institutes of Health (R01-CA202814) to NFS. We acknowledge Dr. Andrzej S. Pitek for help with the preparation of TMV nanoparticles and Dr. Duc H. T. Le for help with western blot analysis.

References

1. Duyn JH. The Future of Ultra-High Field MRI and fMRI for Study of the Human Brain. NeuroImage. 2012; 62:1241–1248. [PubMed: 22063093]
2. Nakada T. Clinical Application of High and Ultra High-Field MRI. Brain Dev. 2007; 29:325–335. [PubMed: 17113259]
3. Das GK, Johnson NJJ, Cramen J, Blasiak B, Latta P, Tomanek B, van Veggel FCJM. $NaDyF_4$ Nanoparticles as T_2 Contrast Agents for Ultrahigh Field Magnetic Resonance Imaging. J Phys Chem Lett. 2012; 3:524–529. [PubMed: 26286058]
4. Merbach, AS., Helm, L. Tóth, É The Chemistry of Contrast Agents in Medical Magnetic Resonance Imaging. John Wiley & Sons; 2013.

5. Caravan P. Strategies for Increasing The Sensitivity of Gadolinium Based MRI Contrast Agents. Chem Soc Rev. 2006; 35:512–523. [PubMed: 16729145]
6. Hu H, Arena F, Gianolio E, Boffa C, Di Gregorio E, Stefania R, Orio L, Baroni S, Aime S. Mesoporous Silica Nanoparticles Functionalized With Fluorescent and MRI Reporters for The Visualization of Murine Tumors Overexpressing $\alpha_v\beta_3$ receptors. Nanoscale. 2016; 8:7094–7104. [PubMed: 26960989]
7. Terreno E, Castelli DD, Viale A, Aime S. Challenges for Molecular Magnetic Resonance Imaging. Chem Rev. 2010; 110:3019– 3042. [PubMed: 20415475]
8. Lee N, Yoo D, Ling D, Cho MH, Hyeon T, Cheon J. Iron Oxide Based Nanoparticles for Multimodal Imaging and Magneto-responsive Therapy. Chem Rev. 2015; 115:10637–10689. [PubMed: 26250431]
9. Viswanathan S, Kovacs Z, Green KN, Ratnakar SJ, Sherry AD. Alternatives to Gadolinium-Based Metal Chelates for Magnetic Resonance Imaging. Chem Rev. 2010; 110:2960–3018. [PubMed: 20397688]
10. Norek M, Peters JA. MRI Contrast Agents Based on Dysprosium or Holmium. Prog Nucl Magn Reson Spectrosc. 2011; 59:64–82. [PubMed: 21600356]
11. Shokrollahi H. Contrast Agents for MRI. Mater Sci Eng, C. 2013; 33:4485–4497.
12. Vander Elst L, Zhang S, Sherry AD, Laurent S, Botteman F, Muller RN. Dy-Complexes as High Field T_2 Contrast Agents. Acad Radiol. 2002; 9:S297–S299. [PubMed: 12188253]
13. Vander Elst L, Roch A, Gillis P, Laurent S, Botteman F, Bulte JWM, Muller RN. Dy-DTPA Derivatives as Relaxation Agents for Very High Field MRI: The Beneficial Effect of Slow Water Exchange on The Transverse Relaxivities. Magn Reson Med. 2002; 47:1121–1130. [PubMed: 12111958]
14. Harris M, Vander Elst L, Laurent S, Parac-Vogt TN. Magnetofluorescent Micelles Incorporating DyIII-DOTA as Potential Bimodal Agents for Optical and High Field Magnetic Resonance Imaging. Dalton Trans. 2016; 45:4791–4801. [PubMed: 26865457]
15. Das GK, Zhang Y, D'Silva L, Padmanabhan P, Heng BC, Chye Loo JS, Selvan ST, Bhakoo KK, Yang Tan TT. Single-Phase Dy_2O_3:Tb^{3+} Nanocrystals as Dual-Modal Contrast Agent for High Field Magnetic Resonance Optical Imaging. Chem Mater. 2011; 23:2439–2446.
16. Norek M, Kampert E, Zeitler U, Peters JA. Tuning of the Size of Dy_2O_3 Nanoparticles for Optimal Performance as an MRI Contrast Agent. J Am Chem Soc. 2008; 130:5335–5340. [PubMed: 18355014]
17. De León-Rodríguez LM, Martins AF, Pinho MC, Rofsky NM, Sherry AD. Basic MR Relaxation Mechanisms and Contrast Agent Design. Magn Reson Imag. 2015; 42:545–565.
18. Huang C-H, Nwe K, Al Zaki A, Brechbiel MW, Tsourkas A. Biodegradable Polydisulfide Dendrimer Nanoclusters as MRI Contrast Agents. ACS Nano. 2012; 6:9416–9424. [PubMed: 23098069]
19. Ratzinger G, Agrawal P, Körner W, Lonkai J, Sanders HMHF, Terreno E, Wirth M, Strijkers GJ, Nicolay K, Gabor F. Surface Modification of PLGA Nanospheres With Gd-DTPA and Gd-DOTA for High-Relaxivity MRI Contrast Agents. Biomaterials. 2010; 31:8716–8723. [PubMed: 20797782]
20. Mariano RN, Alberti D, Cutrin JC, Geninatti Crich S, Aime S. Design of PLGA Based Nanoparticles for Imaging Guided Applications. Mol Pharmaceutics. 2014; 11:4100–4106.
21. An L, Hu H, Du J, Wei J, Wang L, Yang H, Wu D, Shi H, Li F, Yang S. Paramagnetic Hollow Silica Nanospheres for *In Vivo* Targeted Ultrasound and Magnetic Resonance Imaging. Biomaterials. 2014; 35:5381–5392. [PubMed: 24703718]
22. Bruckman MA, Hern S, Jiang K, Flask CA, Yu X, Steinmetz NF. Tobacco Mosaic Virus Rods and Spheres as Supramolecular High-Relaxivity MRI Contrast Agents. J Mater Chem B. 2013; 1:1482–1490.
23. Bruckman MA, Jiang K, Simpson EJ, Randolph LN, Luyt LG, Yu X, Steinmetz NF. Dual-Modal Magnetic Resonance and Fluorescence Imaging of Atherosclerotic Plaques *In Vivo* Using VCAM-1 Targeted Tobacco Mosaic Virus. Nano Lett. 2014; 14:1551– 1558. [PubMed: 24499194]
24. Lin, B., Ratna, B. Virus Hybrids as Nanomaterials - Methods and Protocols. Vol. 1108. Humana Press; 2014. p. 173-185.Chapter 13

25. Culver JN. Tobacco Mosaic Virus Assembly and Disassembly: Determinants in Pathogenicity and Resistance. Annu Rev Phytopathol. 2002; 40:287–308. [PubMed: 12147762]
26. Doshi N, Prabhakarpandian B, Rea-Ramsey A, Pant K, Sundaram S, Mitragotri S. Flow and Adhesion of Drug Carriers In Blood Vessels Depend on Their Shape: A Study Using Model Synthetic Microvascular Networks. J Controlled Release. 2010; 146:196–200.
27. Vácha R, Martinez-Veracoechea FJ, Frenkel D. Receptor-Mediated Endocytosis of Nanoparticles of Various Shapes. Nano Lett. 2011; 11:5391–5395. [PubMed: 22047641]
28. Czapar AE, Zheng Y-R, Riddell IA, Shukla S, Awuah SG, Lippard SJ, Steinmetz NF. Tobacco Mosaic Virus Delivery of Phenanthriplatin for Cancer therapy. ACS Nano. 2016; 10:4119–4126. [PubMed: 26982250]
29. Hu H, Zhou H, Du J, Wang Z, An L, Yang H, Li F, Wu H, Yang S. Biocompatiable Hollow Silica Microspheres as Novel Ultrasound Contrast Agents for *In Vivo* Imaging. J Mater Chem. 2011; 21:6576–6583.
30. Odedina FT, Ogunbiyi JO, Ukoli FAM. Roots of Prostate Cancer in African-American Men. J Natl Med Assoc. 2006; 98:539–543. [PubMed: 16623066]
31. Quinn M, Babb P. Patterns and Trends in Prostate Cancer Incidence Survival, Prevalence and Mortality. Part I: International Comparisons. BJU Int. 2002; 90:162–173. [PubMed: 12081758]
32. Grzesiak JJ, Bouvet M. The $\alpha_2\beta_1$ Integrin Mediates the Malignant Phenotype on Type I Collagen in Pancreatic Cancer Cell Lines. Br J Cancer. 2006; 94:1311–1319. [PubMed: 16622460]
33. Hu H, Li D, Liu S, Wang M, Moats R, Conti PS, Li Z. Integrin $\alpha_2\beta_1$ Targeted $GdVO_4$:Eu Ultrathin Nanosheet for Multi-modal PET/MR Imaging. Biomaterials. 2014; 35:8649–8658. [PubMed: 25043573]
34. Schlick TL, Ding Z, Kovacs EW, Francis MB. Dual-Surface Modification of the Tobacco Mosaic Virus. J Am Chem Soc. 2005; 127:3718–3723. [PubMed: 15771505]
35. Pitek AS, Jameson SA, Veliz FA, Shukla S, Steinmetz NF. Serum Albumin 'Camouflage' of Plant Virus Based Nanoparticles Prevents Their Antibody Recognition and Enhances Pharmacokinetics. Biomaterials. 2016; 89:89–97. [PubMed: 26950168]
36. Soesbe TC, Ratnakar SJ, Milne M, Zhang S, Do QN, Kovacs Z, Sherry AD. Maximizing T_2-exchange in Dy^{3+}DOTA-(amide)X chelates: Fine-Tuning the Water Molecule Exchange Rate for Enhanced T_2 Contrast in MRI. Magn Reson Med. 2014; 71:1179– 1185. [PubMed: 24390729]
37. Rohrer M, Bauer H, Mintorovitch J, Requardt M, Weinmann H-J. Comparison of Magnetic Properties of MRI Contrast Media Solutions at Different Magnetic Field Strengths. Invest Radiol. 2005; 40:715–724. [PubMed: 16230904]
38. Solomon I. Relaxation Processes In a System of Two Spins. Phys Rev. 1955; 99:559–565.
39. Bloembergen N, Morgan LO. Proton Relaxation Times in Paramagnetic Solutions. Effects of Electron Spin Relaxation. J Chem Phys. 1961; 34:842–850.
40. Gueron M. Nuclear Relaxation in Macromolecules by Paramagnetic Ions: A Novel Mechanism. J Magn Reson (1969–1992). 1975; 19:58–66.
41. Vega A0J, Fiat D. Nuclear Relaxation Processes of Paramagnetic Complexes The Slow-Motion Case. Mol Phys. 1976; 31:347–355.
42. Yung KT. Empirical Models of Transverse Relaxation for Spherical Magnetic Perturbers. Magn Reson Imaging. 2003; 21:451–463. [PubMed: 12878254]
43. Wang X, Ma D, Olson WC, Heston WDW. *In Vitro* and *In Vivo* Responses of Advanced Prostate Tumors to PSMA ADC, an Auristatin-Conjugated Antibody to Prostate-Specific Membrane Antigen. Mol Cancer Ther. 2011; 10:1728–1739. [PubMed: 21750220]
44. Hauck TS, Anderson RE, Fischer HC, Newbigging S, Chan WCW. *In vivo* Quantum-Dot Toxicity Assessment. Small. 2010; 6:138–144. [PubMed: 19743433]
45. Chen N, Wang H, Huang Q, Li J, Yan J, He D, Fan C, Song H. Long-Term Effects of Nanoparticles on Nutrition and Metabolism. Small. 2014; 10:3603–3611. [PubMed: 24832525]
46. Song S-K, Qu Z, Garabedian EM, Gordon JI, Milbrandt J, Ackerman JJH. Improved Magnetic Resonance Imaging Detection of Prostate Cancer in A Transgenic Mouse Model. Cancer Res. 2002; 62:1555–1558. [PubMed: 11888935]

47. Banerjee SR, Ngen EJ, Rotz MW, Kakkad S, Lisok A, Pracitto R, Pullambhatla M, Chen Z, Shah T, Artemov D, Meade TJ, Bhujwalla ZM, Pomper MG. Synthesis and Evaluation of GdIII-Based Magnetic Resonance Contrast Agents for Molecular Imaging of Prostate-Specific Membrane Antigen. Angew Chem Int Ed. 2015; 54:10778–10782.

48. Albanese A, Chan WC. Effect of Gold Nanoparticle Aggregation on Cell Uptake and Toxicity. ACS Nano. 2011; 5:5478–89. [PubMed: 21692495]

49. Chen TJ, Cheng TH, Hung YC, Lin KT, Liu GC, Wang YM. Targeted Folic Acid-PEG Nanoparticles for Noninvasive Imaging of Folate Receptor by MRI. J Biomed Mater Res, Part A. 2008; 87A:165–175.

50. Drugs.com. Feridex Dosage. https://www.drugs.com/dosage/feridex.html (accessed Oct 25, 2016)

51. Kumar R, Roy I, Ohulchanskky TY, Vathy LA, Bergey EJ, Sajjad M, Prasad PN. *In Vivo* Biodistribution and Clearance Studies Using Multimodal Organically Modified Silica Nanoparticles. ACS Nano. 2010; 4:699–708. [PubMed: 20088598]

52. Huang CW, Li Z, Cai H, Shahinian T, Conti PS. Novel $\alpha_2\beta_1$ Integrin-Targeted Peptide Probes for Prostate Cancer Imaging. Mol Imaging. 2011; 10:284–294. [PubMed: 21486537]

53. Volpes R, van den Oord JJ, Desmet VJ. Distribution of The VLA Family of Integrins in Normal and Pathological Human Liver Tissue. Gastroenterology. 1991; 101:200–206. [PubMed: 2044908]

54. Xiao G, Wang D, Benson MD, Karsenty G, Franceschi RT. Role of The α_2-Integrin in Osteoblast-Specific Gene Expression and Activation of the Osf2 Transcription Factor. J Biol Chem. 1998; 273:32988–32994. [PubMed: 9830051]

55. Hennig J, Nauerth A, Friedburg H. RARE Imaging: A Fast Imaging Method for Clinical MR. Magn Reson Med. 1986; 3:823–833. [PubMed: 3821461]

56. Chen Y, Li W, Jiang K, Wang CY, Yu X. Rapid T_2 Mapping of Mouse Heart Using the Carr–Purcell–Meiboom–Gill Sequence and Compressed Sensing Reconstruction. J Magn Reson Imaging. 2016; 44:375–382. [PubMed: 26854752]

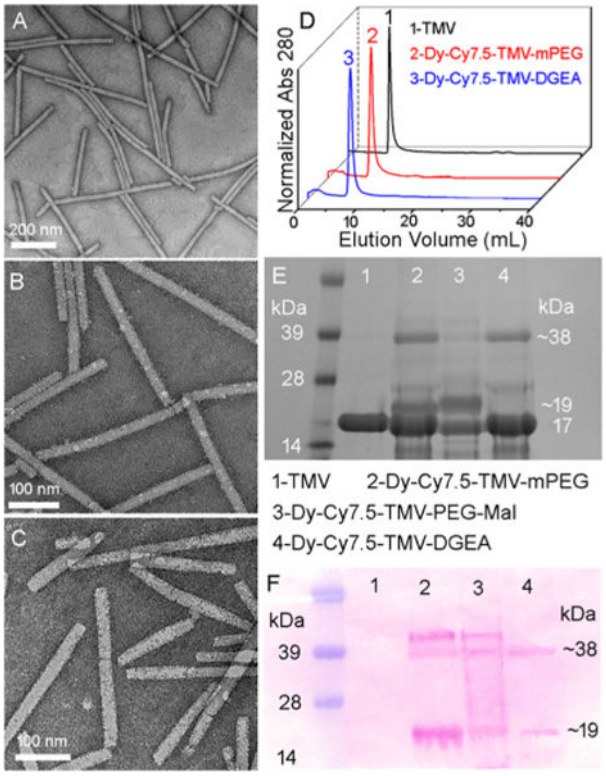

Figure 1.

(A) Low-magnification transmission electron micrograph (TEM) image of native TMV. (B) High-magnification TEM image of Dy-Cy7.5-TMV-mPEG. (C) High-magnification TEM image of Dy-Cy7.5-TMV-DGEA. (D) Size-exclusion chromatography. (E) Sodium dodecyl sulfate polyacrylamide gel electrophoresis. (F) Western blotting analysis of TMV before and after surface modification. The Western blot was probed with anti-PEG antibodies.

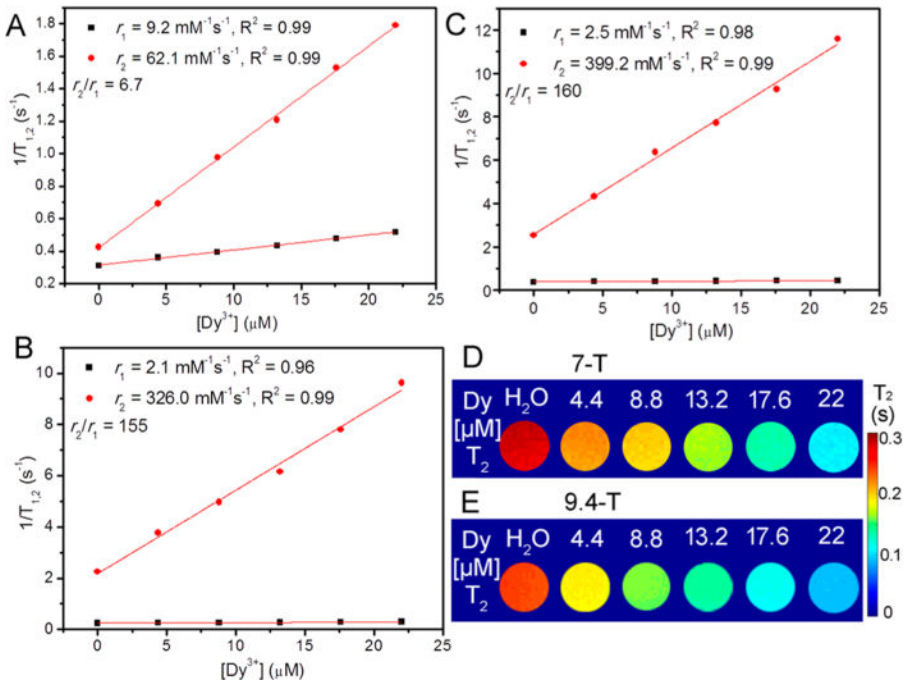

Figure 2.

Water proton longitudinal (r_1) and transversal (r_2) relaxation times of Dy-Cy7.5-TMV-mPEG as a function of Dy^{3+} concentration measured at 37 °C and magnetic fields of (A) 1.5, (B) 7, and (C) 9.4 T. T_2 mapping phantoms of Dy-Cy7.5-TMV-mPEG aqueous solutions at various concentrations of Dy^{3+} obtained in magnetic fields of (D) 7 and (E) 9.4 T.

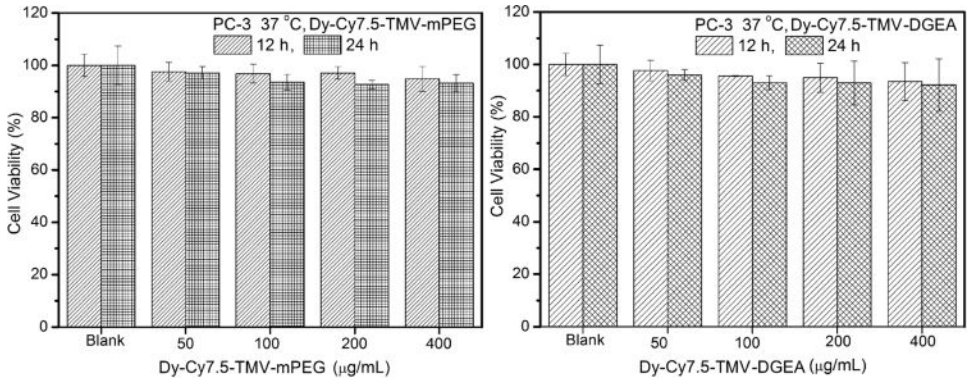

Figure 3.

Viability of a human prostate cancer cell line PC-3 following exposure to different concentrations of (A) Dy-Cy7.5-TMV-mPEG and (B) Dy-Cy7.5-TMV-DGEA for 12 and 24 h.

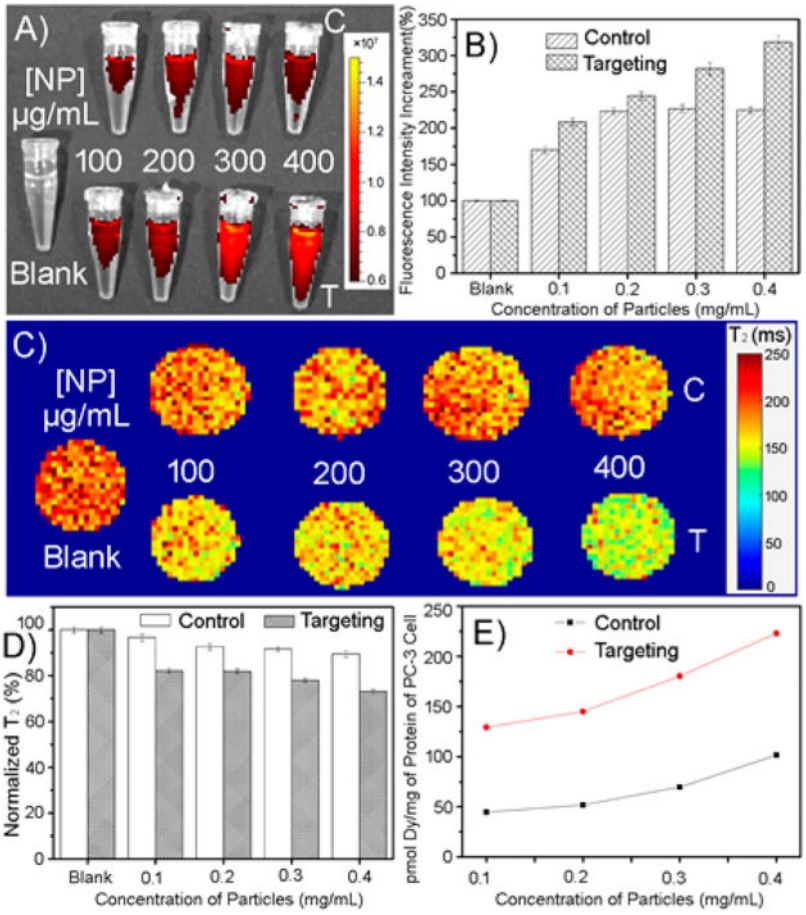

Figure 4.

Analysis of *in vitro* targeting with TMV-based nanoparticles using bimodal imaging. (A) NIRF imaging of PC-3 cells treated with different concentrations of Dy-Cy7.5-TMV-mPEG or Dy-Cy7.5-TMV-DGEA at 37 °C for 3 h. (B) Quantitative analysis of fluorescence intensity. (C) T_2-mapping MRI of PC-3 cells treated with different concentrations of Dy-Cy7.5-TMV-mPEG or Dy-Cy7.5-TMV-DGEA at 37 °C for 3 h. (D) Decrease in T_2 as a function of increasing nanoparticle concentration. (E) Dy^{3+} taken up into PC-3 cells determined by ICP-OES and the Bradford protein assay after MRI.

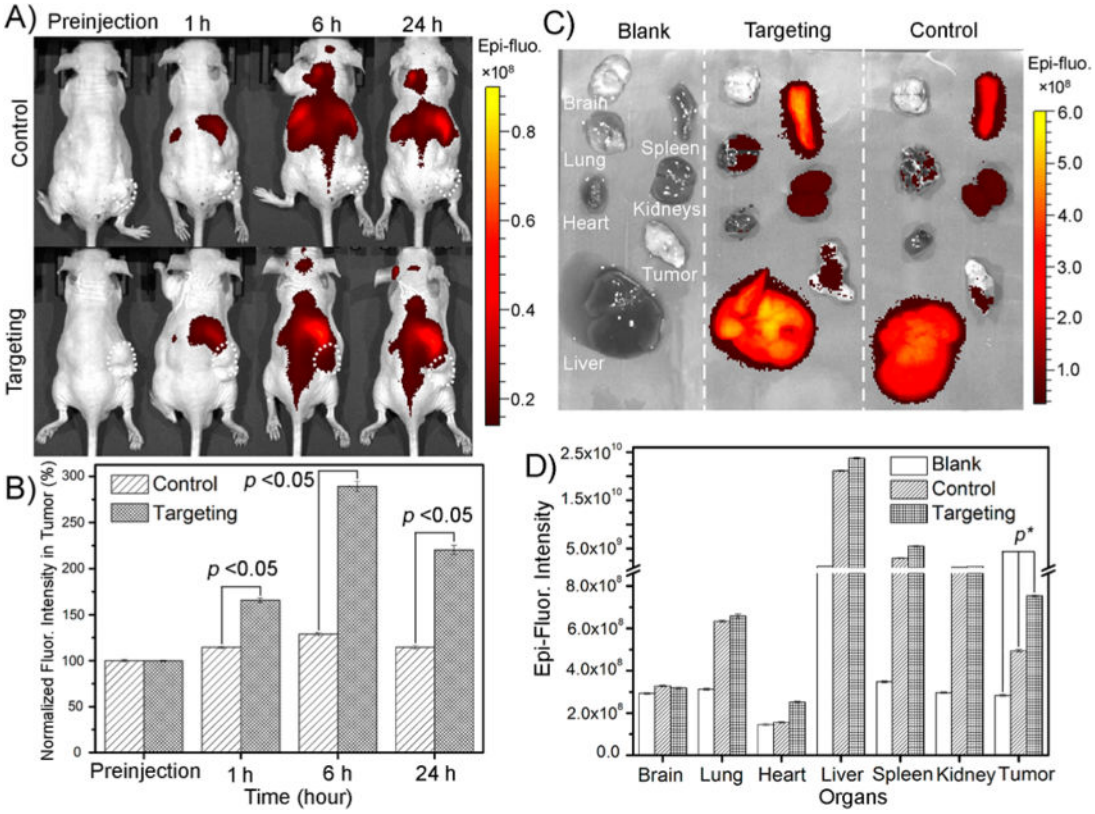

Figure 5.

Near-infrared fluorescence (NIRF) imaging *in vivo*. (A) NIRF images of subcutaneous PC-3 ($\alpha_2\beta_1$) prostate tumors in athymic nude mice ($n = 3$) before and 1, 6, and 24 h after the intravenous injection of Dy-Cy7.5-TMV-mPEG (control group) or Dy-Cy7.5-TMV-DGEA (targeting group). (B) Quantitative analysis of fluorescence intensity in tumors ($p < 0.05$). (C) *Ex vivo* NIRF images of main organs (brain, lung, heart, liver, spleen, kidneys, and tumor) after bimodal scanning (24 h postinjection) and (D) quantitative analysis of fluorescence intensity in each organ based on *ex vivo* NIRF imaging ($p^* < 0.05$ in tumor).

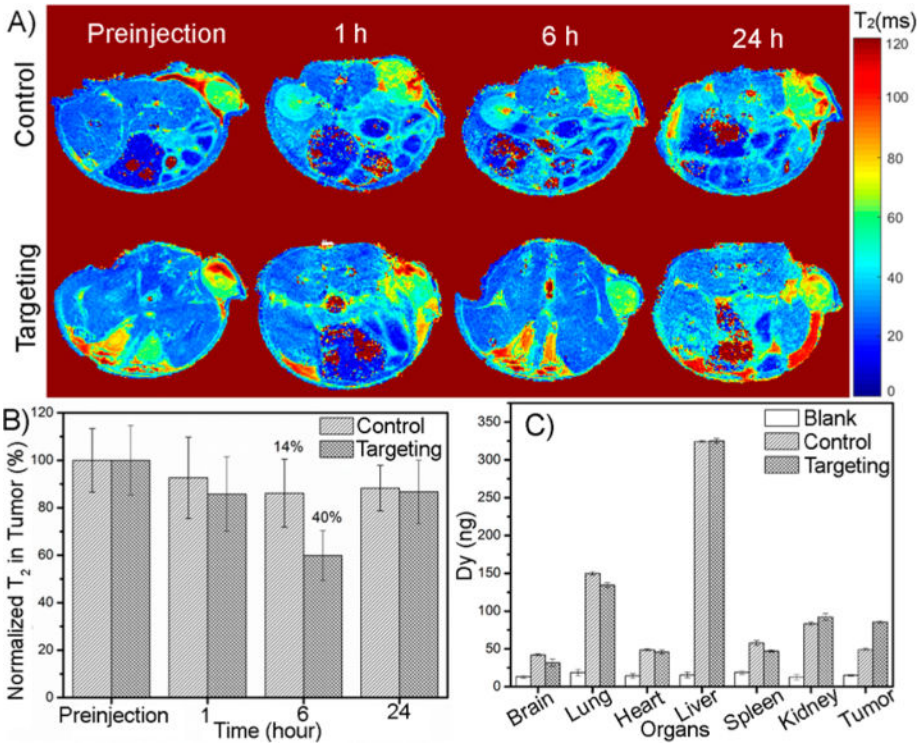

Figure 6.

(A) *In vivo* T_2-mapping MRI of subcutaneous PC-3 ($\alpha_2\beta_1$) prostate tumors in athymic nude mice ($n = 3$) obtained before and 1, 6, and 24 h after the intravenous injection of Dy-Cy7.5-TMV-mPEG (control group) and Dy-Cy7.5-TMV-DGEA (targeting group). (B) Quantitative analysis of T_2 reduction in tumors. (C) Biodistribution of Dy^{3+} in the main organs of mice after bimodal scanning (24 h postinjection).

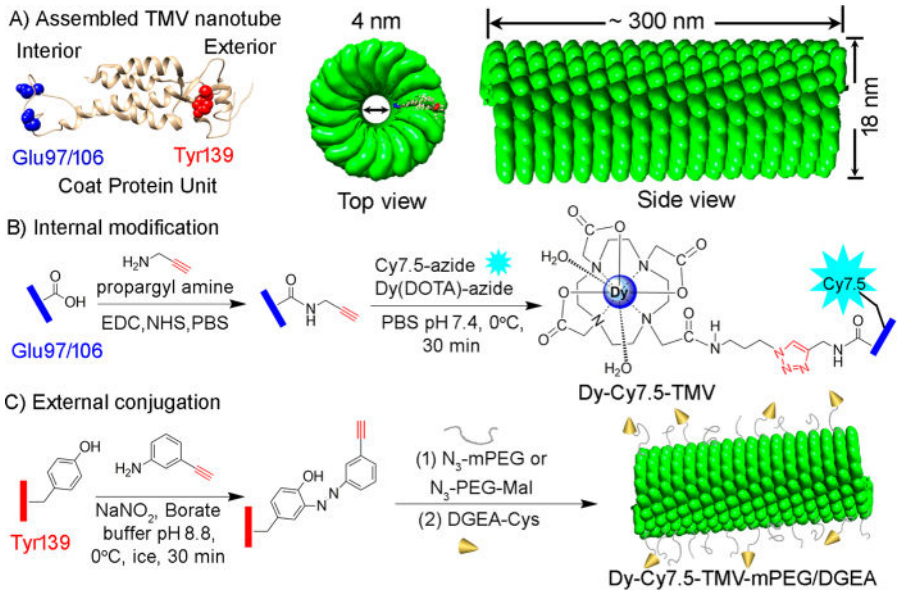

Scheme 1.

(A) Structure of the Tobacco Mosaic Virus (TMV) Nanoparticle's Coat Protein with Surface-Exposed Residues Highlighted as Internal Glutamic Acid (Blue) and External Tyrosine (Red) and the Structure of the Assembled Capsid. (B) Strategy for Internal Modification. (C) Strategy for External Modification[a]

[a]Images were created using UCSF Chimera software, PDB entry 2TMV, and ChemDraw v15.0.